Rare Met. (2025) 44(11):9144–9158
https://doi.org/10.1007/s12598-025-03582-7

RARE METALS

ORIGINAL ARTICLE

# Biomedical Ti–Zr–Mo–Cu medium-entropy alloys with excellent mechanical and antibacterial properties by various quenching processes

**Zhi-Jun Guo, Yu-Sha Luo, Min-Qi Xu, Min-Tao Xue, Bian-Yun Cai, Yi-Zhou Huang*, Bao-Long Shen***

Received: 9 April 2025 / Revised: 18 July 2025 / Accepted: 22 July 2025 / Published online: 1 September 2025


**Abstract** The development of medium-entropy alloys (MEAs) with superior mechanical properties and remarkable antibacterial performance has garnered significant attention in the field of metallic biomaterials. In this study, Ti–18Zr–8Mo–10Cu MEAs with varying properties, including mechanical properties, corrosion resistance, antibacterial performance, and cytocompatibility, were obtained through heat treatment at 900 °C for 1 h, followed by various cooling methods (water cooling, air cooling, and furnace cooling). An increasing cooling rate results in a decrease in the elastic modulus. The water-cooling specimen exhibits optimal ductility over 40% and minimum elastic modulus of 60 GPa. Moreover, the reduction in alloy composition segregation after heat treatment enhances the anticorrosion properties, exhibiting a robust passivation capability of MEAs. All synthesized Ti–18Zr–8Mo–10Cu MEAs show favorable cytocompatibility and robust antibacterial rate approaching ~ 100% at 12 and 24 h. Generally, the water-cooling specimen shows exceptional mechanical properties and outstanding antibacterial performance, holding considerable promise for future orthopedic applications. This study offers a viable approach to optimizing the comprehensive properties of copper-bearing Ti MEAs for biomedical applications.

**Keywords** Biomedical medium-entropy alloys; Cooling method; Mechanical property; Antibacterial performance; Biomedical application

Zhi-Jun Guo and Yu-Sha Luo have contributed equally to this work.

**Supplementary Information** The online version contains supplementary material available at https://doi.org/10.1007/s12598-025-03582-7.

Z.-J. Guo, Y.-S. Luo, M.-Q. Xu, B.-L. Shen*
School of Materials Science and Engineering, Jiangsu Key Laboratory for Advanced Metallic Materials, Southeast University, Nanjing 211189, China
e-mail: blshen@seu.edu.cn

M.-T. Xue
Department of Orthopedics, Second Affiliated Hospital, Naval Medical University, Shanghai 200003, China

B.-Y. Cai
School of Medical Technology and Engineering, Henan University of Science and Technology, Luoyang 471023, China

Y.-Z. Huang*
Sports Medicine Center, West China Hospital, Sichuan University, Chengdu 610041, China
e-mail: huangyizhou@wchscu.cn

Y.-Z. Huang
Department of Orthopedic Surgery and Orthopedic Research Institute, West China Hospital, Sichuan University, Chengdu 610041, China

## 1 Introduction

Titanium (Ti) alloys are extensively employed as metallic biomaterials owing to their superior mechanical properties, corrosion resistance, and biocompatibility [1]. They are classified into three categories based on their constituent phases: α, α + β, and β types. Compared to α and α + β type Ti alloys, many β type Ti alloys demonstrate improved mechanical properties, notably a reduced elastic modulus, which could address the long-standing issue of "stress shielding" in bone–implant application to align with that of natural bone. However, most traditional β-Ti alloys inaccessibly possess inherent antibacterial activity, a vital characteristic for the prevention of postoperative

infections, and accompany the occurrence of high-modulus phase transformation.

From a clinical perspective, infections related to metallic orthopedic implants represent the second most common cause of postoperative complications [2], because traditional metallic implants, such as Ti–6Al–4 V and Co–Cr–Mo, are lack of antibacterial ability [3, 4]. The incidence of postoperative infections following arthroplasty procedures is estimated to be 0.5%–2% for knees, 0.3%–1.7% for hips, and 2%–9% for ankle replacements [5, 6]. In the USA, bacterial infections are responsible for the failure of 4.3% of orthopedic implants each year [7], resulting in substantial economic burdens on society [8, 9]. An effective strategy to mitigate the incidence of bacterial infections associated with metallic implants involves imparting robust antibacterial properties that inhibit bacterial adherence [10]. Various surface modification techniques have been employed to enhance the antibacterial properties of alloys, including the deposition of silver nanoparticles [11], sol–gel synthesis of antibacterial coatings [12], and plasma spraying of copper (Cu) coating [13]. These methods present certain limitations, such as the peeling or dissolution of coatings, which may compromise the antibacterial efficacy of implants once they are placed in the body. To attain a more stable antibacterial effect, the development of new Ti alloys incorporating metallic elements with inherent antibacterial properties, such as Cu, silver, and tin, has attracted considerable interest. Copper, an essential trace element in the human body, has been employed as an effective antibacterial agent due to its antimicrobial capabilities [14]. As reported, the Cu-bearing Ti alloys, including Ti–Cu alloys [15], Ti–6Al–4 V–*x*Cu alloys [16], and Ti–13Nb–13Zr–10Cu alloys [17], demonstrate favorable antibacterial properties. However, there are concerns regarding the potential reduction in mechanical strength and the release of toxic ions (e.g., aluminum and vanadium in Ti-6Al-4 V or Ti–6Al–4 V–*x*Cu alloys).

Recently, high- and medium-entropy alloys (HEAs/MEAs) have obtained significant attention as advanced functional materials. The core attributes of HEAs/MEAs—namely, high entropy, lattice distortion, sluggish diffusion, and cocktail effects—contribute to their exceptional properties, including high strength, excellent wear resistance, and corrosion resistance [18–20]. The performance of HEAs can be tailored through compositional design, thereby offering substantial potential to address the limitations of traditional Ti alloys. Although HEAs with high yield strength (800–1600 MPa), good plasticity, and excellent wear resistance have been explored, such as Ti–Zr–Hf–Nb–Ta [21, 22], Ti–Nb–Ta–Zr [23], and Ti–Zr–Hf–Cr–Mo [24], for biomedical applications, their elastic moduli remain significantly higher than that of human bone (10–30 GPa). In contrast, MEAs may achieve low elastic modulus [25–27] while retaining the aforementioned combination property.

In this study, we focused on MEAs with a low elastic modulus, outstanding corrosion resistance and biocompatibility. Ti–18Zr–8Mo–10Cu alloy was selected as our prototype alloy. This elemental synergy enables concurrent optimization of antimicrobial efficacy (via Cu), phase stability (via Mo), and mechanical reinforcement (via Zr), aligning with the tripartite requirements of bone–implant materials: biomechanical compatibility, structural durability, and infection resistance. In addition, the control of cooling rates during thermal processing provides a critical strategy for β-phase stabilization in biomedical MEAs. Rapid quenching from the β-phase field (typically > 850 °C) effectively retaining the metastable β structure while inhibiting precipitation of high-modulus phases. Overall, our study establishes a fundamental basis for the creation of bio-MEAs.

## 2 Experimental

### 2.1 Material preparation

Ingots with a nominal composition of Ti–18Zr–8Mo–10Cu (wt%) were synthesized through vacuum arc melting of Ti, Zr, Mo, and Cu rods, each with a purity of at least 99.95 wt%, under an argon protective atmosphere. To ensure complete homogeneity, the ingots underwent a minimum of six melting cycles. The resultant as-cast alloy, referred to as the AS alloy, was characterized as a metastable β-Ti alloy with a phase transition temperature of 873 °C [28, 29]. Different annealing treatments were designed to investigate the influence of cooling methods on the comprehensive properties of alloys. Briefly, the as-cast alloy underwent heat treatment in a muffle furnace at 900 °C for 1 h, followed by cooling through different methods, namely, water cooling, air cooling, or furnace cooling to produce samples with distinct initial microstructures. The cooling rate achieved during water cooling was not less than 1000 °C $min^{-1}$, whereas air cooling exhibited rates ranging from approximately 15–30 °C $min^{-1}$, and furnace cooling was conducted at a rate of 5 °C $min^{-1}$. After heat treatment, the oxide layers that formed on the alloy surfaces were removed by polishing. The samples were designated by abbreviations indicative of the employed cooling methods: the furnace cooling (FC) alloy, the air cooling (AC) alloy, and the water-cooling (WC) alloy. Commercially pure Ti was used as the control sample.

### 2.2 Microstructure observation

To identify the constituent phases of alloy samples, X-ray diffraction (XRD) analysis was performed using an X-ray

diffractometer (D8 Discover, Bruker, Germany) equipped with Cu-Kα radiation. The operational parameters included a tube voltage of 50 kV, a scanning step size of 0.02°, a scanning rate of 0.15 s per step, and a scanning angle range from 30° to 90°. Before testing, the samples were polished with 400-, 800-, and 1000-grit sandpaper, followed by a 5-min ultrasonic cleaning. Data analysis and processing were conducted using JADE software, which facilitated the identification of the phase composition and crystal structure of alloys.

The microstructure and fracture morphology of alloys were examined using a field emission environmental scanning electron microscope (SEM; Nova nano 450, FEI, USA) equipped with X-ray energy-dispersive spectroscopy (EDS). EDS was utilized to analyze the composition of samples. The sample preparation procedure was as follows: Initially, the samples were polished using 800-, 1000-, 1500-, and 2000-grit sandpaper. Subsequently, they were polished with a 50 μm silica polishing fluid until the surface was bright and free of scratches. Thereafter, chemical etching was performed using Kroll's reagent ($HF:HNO_3:H_2O$ = 2:1:17) for 5–30 s, after which the samples were rinsed with ethanol and dried.

The microstructure, electron diffraction pattern, and compositional distribution of alloys at the nanoscale were investigated using transmission electron microscopy (TEM; Talos F200X, Thermo Fisher, USA). Sample preparation involved several steps: Initially, a thin sheet with a thickness of 0.3 mm was produced using wire electrical discharge machining. Subsequently, the sample was ground on both sides to achieve a thickness in the range of 30–50 μm, utilizing 1000- and 2000-grit sandpapers. This process was followed by ion thinning treatment (GATAN-M691), where a 5 keV ion beam was applied until micro holes appeared in the center of the sample. Thereafter, a 4 keV ion beam was employed, and the angle was reduced for 15 min to obtain a region of optimal thinness.

## 2.3 Mechanical test

The compression test was performed using a universal testing instrument (Instron 5982, Instron Corp., USA) at a strain rate of $10^{-3}$ $s^{-1}$ and at room temperature. The size of the specimen was ϕ 2 mm × 4 mm. The test was concluded either upon specimen failure or when deformation surpassed 40%. Three specimens were tested for each condition, and the elastic modulus was calculated from the stress–strain curve.

The Vickers microhardness test was conducted utilizing a microhardness tester (FM-700, Future Tech Corp., Japan), with an applied load of 300 g and a dwell time of 10 s, maintaining a spacing of 200 μm between each indentation. Before testing, the samples were subjected to sanding, polishing, and ultrasonic cleaning. The microhardness values were determined by measuring the diagonal lengths of the indentations. To ensure the reliability of results, more than six replicates were performed for each sample.

## 2.4 Electrochemical corrosion test

Corrosion resistance was evaluated in simulated body fluid (SBF) at 37 °C using an electrochemical workstation (Interface1000, Gamry, USA). The experimental setup comprised a working electrode, an auxiliary electrode, and a reference electrode. A saturated calomel electrode (SCE) served as the reference electrode, platinum was utilized as the counter electrode, and the alloy sample functioned as the working electrode. All specimens were processed to a uniform size of ϕ 10 mm × 2 mm, with an exposed surface area of 0.785 $cm^2$, while the remaining surface was coated with epoxy.

Measurements of open-circuit potentials (OCP) were conducted for 1 h until stabilization was achieved. Subsequent electrochemical tests were performed under stable OCP conditions. For the electrochemical impedance spectroscopy (EIS) analysis, a sinusoidal AC voltage of 10 mV was applied, with the scanning frequency range set between 0.01 and 105 Hz. The resulting data were analyzed using Zview software. Following the EIS analysis, a potentiodynamic polarization test was conducted at a scan rate of 0.5 mV $s^{-1}$, covering a potential range from −1 to 1.5 V. Ti served as the control group. All tests were repeated a minimum of three times to ensure the reliability of the data.

## 2.5 Antibacterial performance

### 2.5.1 Antibacterial rate

After grinding the test surface with sandpaper to a grit size of 1000, the surface was polished, followed by ultrasonic cleaning with ethanol for 20 min, and subsequently sterilized at 121 °C for 20 min. The samples (ϕ 10 mm × 2 mm, $n$ = 3 in each group) were placed in a 24-well culture plate, and 50 μL of *E. coli* suspension at the concentration of $10^5$ colony-forming units per mL (CFU $mL^{-1}$) was inoculated onto the surface of each sample. The alloy samples were cultured in Luria–Bertani Broth (Sigma-Aldrich, USA) at 37 °C for 3, 12, and 24 h, respectively. After incubation, the bacterial suspension was harvested and diluted to a concentration of (1.0–10.0) × $10^3$ CFU $mL^{-1}$. Subsequently, 50 μL of the diluted suspension was cultured on agar plates at 37 °C for 24 h. The bacterial colonies were counted, and the

antibacterial efficacy of alloys was determined using the following formula: antibacterial rate (%) = ($N_{control}$–$N_{experiment}$)/$N_{control}$ × 100%, where $N_{control}$ and $N_{experiment}$ denote the average number of bacterial colonies in the control group (i.e., Ti) and the Ti–18Zr–8Mo–10Cu alloys, respectively.

#### 2.5.2 Bacteria observation

Following sterilization, the alloy samples were inoculated with 50 μL of an *E. coli* suspension at the concentration of 106 CFU $mL^{-1}$ and incubated for 24 h. Subsequently, the sample surfaces were gently washed three times with PBS, immersed in 2.5% glutaraldehyde at 4 °C for 4 h, and then dehydrated using a gradient ethanol series (50%, 60%, 70%, 80%, 90%, 95%, and 100%) for 10 min at each concentration. The samples were then air-dried at room temperature. After gold sputtering, the bacterial morphology was examined using scanning electron microscopy (SEM; Nova nano 450, FEI, USA).

Live/dead staining was employed to assess the viability of bacteria adhered to the surface of alloys. Specifically, the alloy samples were incubated with 50 μL of *E. coli* suspension at the concentration of $10^6$ CFU $mL^{-1}$ for 24 h. Following incubation, each sample was gently rinsed with PBS and subsequently stained with SYTO-9 and propidium iodide (Invitrogen, Eugene, OR, USA) in the dark for 20 min. After staining, the samples were gently rinsed with PBS and observed using a confocal laser scanning microscopy (CLSM; TCS SP8, Leica, Germany).

### 2.6 Cytocompatibility of alloys

#### 2.6.1 Cell proliferation

MC3T3-E1 cells were cultured in alpha-minimum essential medium (Gibco, Life Technologies, USA) supplemented with 10% fetal bovine serum (Gibco, Life Technologies, USA) and 1% penicillin–streptomycin (Gibco, Life Technologies, USA). Cell proliferation was assessed using the Cell Counting Kit-8 (CCK-8; Dojindo, Japan). Briefly, the alloy samples were placed in 48-well plates, and 3 × $10^3$ cells were seeded on the surface of the alloy. After culture for 1, 3, and 7 days, the cell culture medium was replaced with 700 μL of CCK-8 work solution and incubated at 37 °C for 2 h. Subsequently, 100 μL of the incubated solution was transferred to a 96-well plate, and absorbance at 450 nm was measured using a microplate reader. Cell viability was determined using the following formula: Cell viability (%) = $OD_{450}$/(sample)$OD_{450}$(control) × 100%, where $OD_{450}$(sample) and $OD_{450}$(control) represent the optical density (OD) measurements at 450 nm for Ti–18Zr–8Mo–10Cu alloys and Ti, respectively. The toxicity grade of the samples was evaluated by the 4-grade toxicity rating standard as specified in GB/T 16886.5–2017.

#### 2.6.2 Cell morphology

After being cultured with MC3T3-E1 cells for 24 h, the alloy samples were fixed in 3.75% formaldehyde for 15 min and subsequently permeabilized with 0.5% Triton X-100 for 10 min at room temperature. The cells were then stained with SF488-labeled phalloidin (Solarbio, China) and 4′,6-diamidino-2-phenylindole (DAPI; Invitrogen, USA) for 20 min at room temperature. Finally, the nuclei and cytoskeleton of cells were observed using a CLSM (TCS SP8, Leica, Germany).

### 2.7 Statistical analysis

All quantitative data are presented as the mean ± standard deviation. Statistical analyses were conducted using GraphPad Prism 9.0 software (GraphPad Software, USA). Differences between groups were assessed using a one-way ANOVA test, with a significance threshold set at $P < 0.05$.

## 3 Results and discussion

### 3.1 Microstructures and phase identifications

Heat treatment significantly influences the microstructure of alloys, such as grain size, phase content, and the distribution of alloying elements. The crystalline structure of the as-cast and annealing MEAs is determined by XRD, as displayed in Fig. S1. A dual-phase structure consisting of β-Ti (body-centered cubic, BCC) and ZrCu phases is identified from XRD spectrum in the as-cast (AS) Ti-18Zr-8Mo-10Cu MEA. After annealing, the furnace-cooled (FC) alloy exhibits multiple phase structures, containing β-Ti, ZrCu, and α-Ti (hexagonal close-packed, HCP) phases. As increasing cooling rate, α-Ti phases are inhibited, and the small peaks corresponding to ZrCu phases can be detected in the air-cooled (AC) alloy. Those ZrCu peaks somewhat become weak indicating the decreasing volume fraction of ZrCu phases. At a higher cooling rate (water-cooled alloy, WC), the characteristic BCC peaks, a key phase structure for exploring the ultra-low elastic modulus and decent ductility of metastable bio-MEAs, can only be identified.

Backscattered electron (BSE) images showing the initial microstructures of AS, FC, AC, and WC alloys are given in Fig. 1. The previous studies have shown that the bright and dark regions correspond to the β-Ti and α-Ti phases, respectively [30]. The β-Ti (Fig. 1A, B) appears as the dendritic structure, indicating the redistribution of

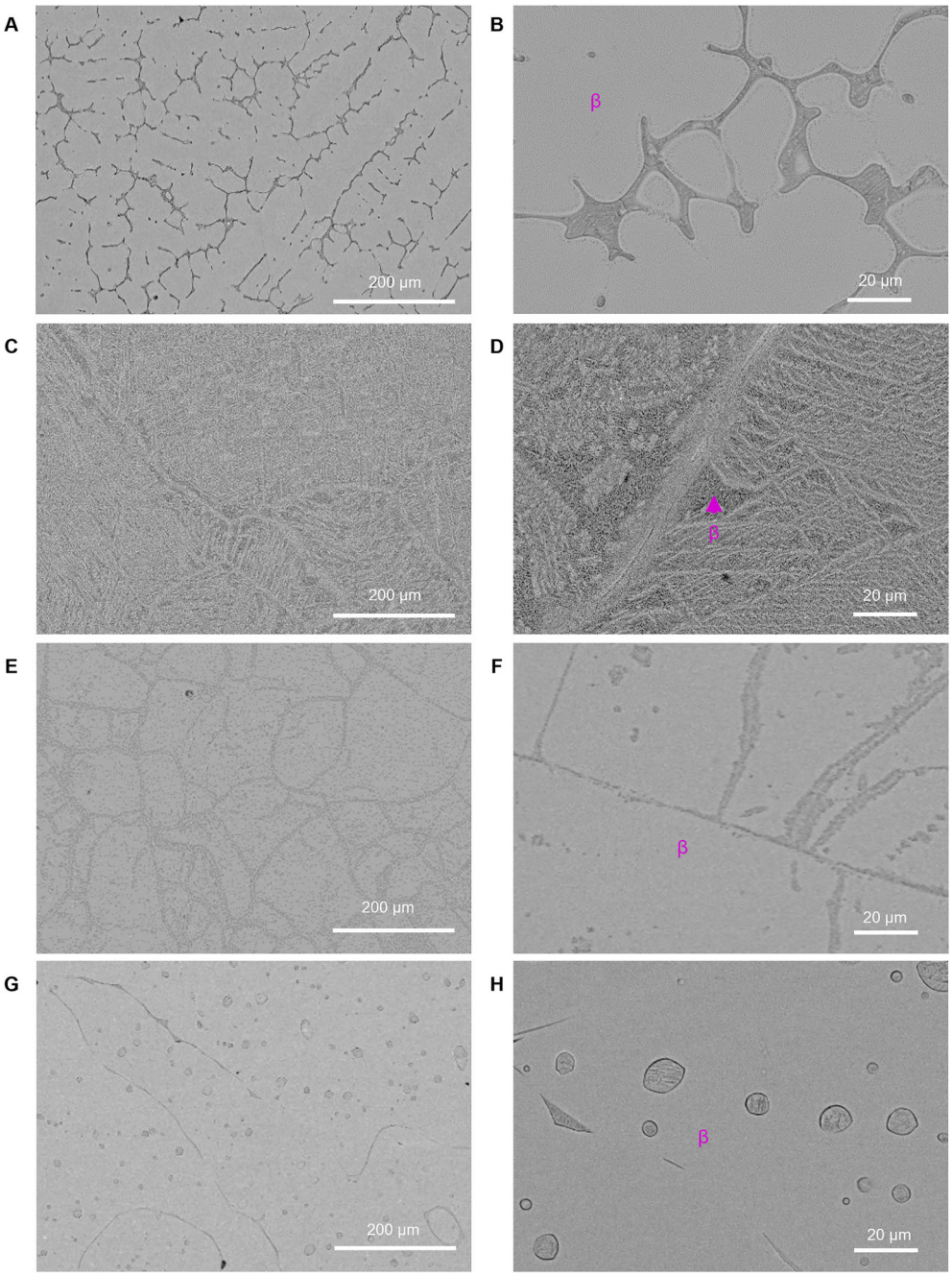


**Fig. 1** Microstructural information of the Ti–18Zr–8Mo–10Cu MEAs. **A**, **B** Backscattered electron (BSE) images of the as-cast (AS) alloy, **C**, **D** FC alloy, **E**, **F** AC alloy, and **G**, **H** WC alloy

constituent elements during solidification in the AS alloys. This equiaxial dendrite structures are analogous to those observed in biomedical HEAs, such as TiNbTaZrMo alloys [23, 31], as well as $Ti_{1.4}Zr_{1.4}Nb_{0.6}Ta_{0.6}Zr_{0.6}$, Ti1.7NbTaZrMo$_{0.5}$, and $Ti_{1.5}$NbTaZrMo$_{0.5}$ alloys [32]. There are needle-shaped precipitates (Fig. 1C, D) in the β-phase with hundreds of nanometers in the FC alloy. In the AC alloy (Fig. 1E, F), some precipitates in a lamellar shape are formed near the grain boundaries, exhibiting refined grains. The single- and double-seam morphology indicates that these precipitates nucleate from grain boundaries and then grow into grains. In the WC alloy, conspicuous particles intersperse in the β matrix (Fig. 1G, H). These findings mean that heat treatment has tailored the microstructure

and elemental distribution of Ti–18Zr–8Mo–10Cu MEAs, potentially impacting their mechanical properties and antibacterial efficacy.

To further examine the microstructures, TEM and selected area electron diffraction (SAED) analyses were performed on Ti–18Zr–8Mo–10Cu MEAs. Figure 2A shows a typical bright-field TEM image of the precipitates in the AS alloy, combined with efforts of the EDS image in Fig. 2C. SAED (Fig. 2B) collected from the zone axis paralleled to [001] (matrix) demonstrates the BCC crystal structure of the β-Ti matrix. Furthermore, compositional analysis using the EDS indicates that the Zr and Cu elements have a strong tendency to partition into the precipitates (marked as ZrCu intermetallic in Fig. 2), whereas Ti and Mo elements are more likely to stay inside the β-Ti matrix. This observation supports the preferential interaction between Cu and Zr, aligning with the findings derived from XRD and SEM results. Similarly, Fig. 2D shows the high-angle annular dark field (HAADF) image of the variform precipitates in the FC MEA. Figure 2E–G presents the diffraction patterns acquired from β matrix, ZrCu, and α-Ti phases, demonstrating the BCC, monoclinic [33], and HCP structures, respectively. The corresponding EDS maps (Fig. 2H) show the segregation of Ti on the α-Ti phases, and the enrichment of Zr, and Cu in the intermetallic, matching well with the above results. In addition, the TEM image (Fig. 3A) of the AC alloy exhibits distinct strip-shaped bands in the β matrix, with an enlarged view (Fig. 3B, C) revealing the presence of β-Ti and ZrCu phases. A high-resolution (HR) TEM image along the $[001]_{\beta}/[1\bar{1}2]_{ZrCu}$ direction unveils a fully coherent crystallographic relationship with the BCC matrix (Fig. 3D). Chemically, the ZrCu phases exhibit a subtle compositional difference from the matrix, as displayed in one-dimensional concentration profiles (Fig. 3E). At the highest cooling rate (the WC alloy, Fig. 3F, G), no nanoscale precipitated phase is detected. These findings further confirm that cooling rates play a crucial role in the phase structures and precipitation behavior in Ti–18Zr–8Mo–10Cu MEAs.

### 3.2 Mechanical properties and corrosion properties

Uniaxial compression tests were performed at room temperature to study the deformation behavior of the specimen before and after annealing. Figure 4A displays the engineering stress–strain curves of Ti–18Zr–8Mo–10Cu MEAs. It is evident that the FC and AC alloys exhibit higher strength, with a yield stress of ∼ 1200 MPa, but along with considerable plasticity loss as compared to the AS and WC alloys (Fig. 4B). The elastic modulus of the MEAs was measured using the linear portion of the elastic stage [33]. The WC alloy shows notably the lowest elastic modulus (∼ 55 GPa) and microhardness (∼ 330 HV) of the bio-MEAs compared to FC and AC alloys (∼ 77 GPa and ∼ 400 HV) in Fig. 4C. It is known that the elastic modulus of Ti–Al–V and Co–Cr–Mo alloys is 114 GPa and 283 GPa, respectively, which are much higher than that of cortical bone (10–30 GPa) [34]. Therefore, all Ti–18Zr–8Mo–10Cu MEAs prepared in this study possessed a superior elastic modulus for orthopedics applications, which was much closer to that of cortical bone.

The low elastic modulus is mainly attributed to the β-phase stability in the WC alloy. As the previous study, the reduction of β-phase stability generally leads to the information of non-equilibrium phases, e.g., athermal αω, ω phases [29], which will dramatically increase the elastic modulus of the bio-MEAs [35]. Therefore, quantitative analysis of second-phase volume fractions was performed on a minimum of ten SEM and TEM micrographs per alloy condition using ImageJ software. The WC alloy exhibited the lowest volume fraction of high-modulus second phases at 1.29%, followed by the AS alloy at 10.59%, the AC alloy at 27.96%, and the FC alloy at 39.48%. Obviously, a progressive reduction in elastic modulus was observed with decreasing second-phase volume fraction, establishing a direct correlation between microstructural evolution and mechanical properties.

After immersion in SBF, the OCP curve reached stabilization (Fig. 4D), which is attributed to the formation and subsequent stabilization of passivation film on the surfaces. As reported, in the design of alloys with non-equiatomic ratios, more elements enhance the stability of the passive oxide layer, such as Zr and Mo [27, 36]. As depicted in Fig. 4E, all Ti–18Zr–8Mo–10Cu MEAs exhibit self-passivation, with indistinct activation–passivation transition zones, suggesting a robust passivation capability of these alloys. The passivation zones observed in the AC and WC alloys are uniform and wide, indicating the formation of a stable passivation film on the surfaces. The previous studies have shown that the passivation behavior of Ti alloys is associated with the oxide film that forms on the alloy surface during the corrosion process. This oxide film, primarily composed of $TiO_2$, effectively inhibits the interaction between the alloy surface and the corrosive environment [37]. Additionally, the presence of pitting corrosion in the FC alloy is indicated by a notable rise in current density at a potential of around 0.735 V, probably due to the potential differences between various phases. Similar pitting behavior also occurs in Ti–Zr–Hf–Nb–Ta [21].

Table S1 shows the electrochemical performance parameters calculated from the curves. All Ti–18Zr–8Mo–10Cu MEAs exhibit a higher corrosion potential ($E_{corr}$)

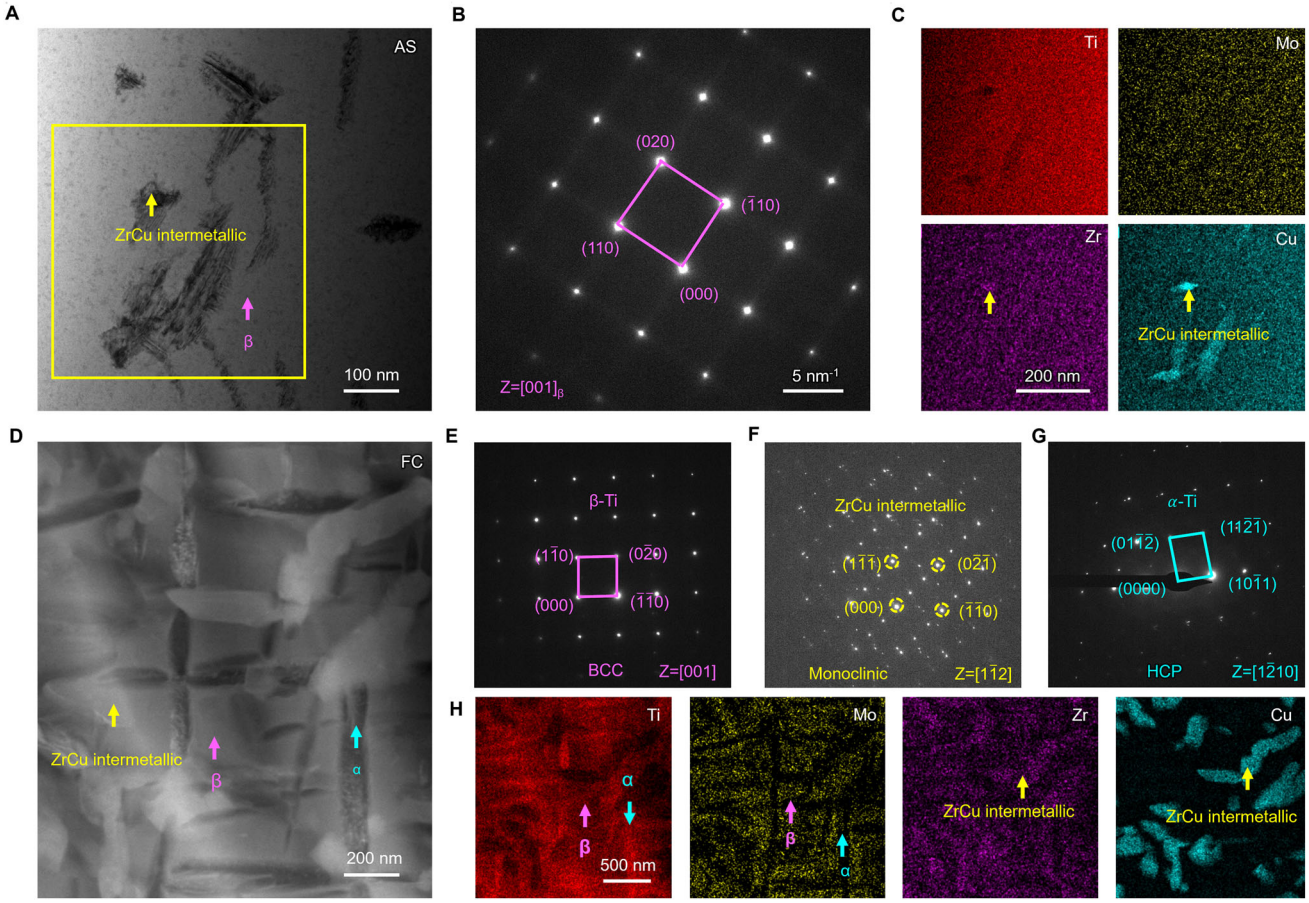


**Fig. 2** TEM characterization of the AS and FC alloys. **A** Bright-field (BF) image, showing submicron precipitates within the β-phase. **B** SAED patterns along $[001]_\beta$ axes for BCC structure. **C** EDS maps of Ti, Mo, Zr, and Cu correspond to the red box in **A**. TEM characterization of the FC alloy. **D** HAADF image and the corresponding SAED patterns of **E** β-Ti, **F** ZrCu intermetallic, and **G** α-Ti phase, respectively. **H** EDS maps of Ti, Mo, Zr, and Cu from **D**

compared to Ti. Except for the AS alloy, all Ti–18Zr–8Mo–10Cu MEAs show a significant reduction in both corrosion current density ($I_{corr}$) and passive current density ($I_{pass}$) relative to Ti, which can be attributed to the reduction of composition segregation. Yang et al. reported that the elements within the Ti–Zr–Hf–Nb–Ta alloy are uniformly distributed, which facilitates the formation of homogeneous protective passive films composed of chemically stable oxides on the surfaces [21]. The lamellar $Ti_2Cu$ phases precipitated in the Ti–7Cu alloy exhibit poor corrosion resistance [38], primarily because of the considerable potential difference ($\Delta V$ = 295 mV) between the α-phase and the $Ti_2Cu$ phase.

Figure 4F presents the Nyquist diagrams of Ti–18Zr–8Mo–10Cu MEAs, where all alloys display a single capacitive loop with a larger circular arc compared to Ti. Larger circular arc is correlated to a larger charge transfer resistance [39], suggesting that heat treatment markedly enhances the corrosion resistance of MEAs. The WC alloy shows the largest charge transfer resistance. To quantitatively substantiate the EIS results, impedance parameters are analyzed using ZView® software, employing the equivalent circuit model proposed by Pan et al. [40]. Table S2 summarizes decreasing resistance values ($R_b$) in the AC, WC, Ti, FC, and AS alloys, which is consistent with the polarization curve results. Using the formula $CR = KI_{corr}EW/\rho$, where $K$ is a constant of $3.27 \times 10^{-3}$, EW is the equivalent weight, and $\rho$ is the density of alloy, the corrosion rates of our alloys are evaluated. The corrosion current density ($I_{corr}$), determined by Tafel extrapolation from potentiodynamic polarization curves, is 0.00495 μA $cm^{-2}$ for WC alloy. The EW and $\rho$ are 14.39 g $equivalent^{-1}$ and 5.62 g $cm^3$, respectively. Therefore, the corrosion rate of the WC alloy is $4.15 \times 10^{-5}$ mm $year^{-1}$, which is much lower than that of Ti–6Al–4 V [41]. Accordingly, it can be inferred that the AC and WC alloys exhibit superior corrosion resistance than AS and Ti alloys.

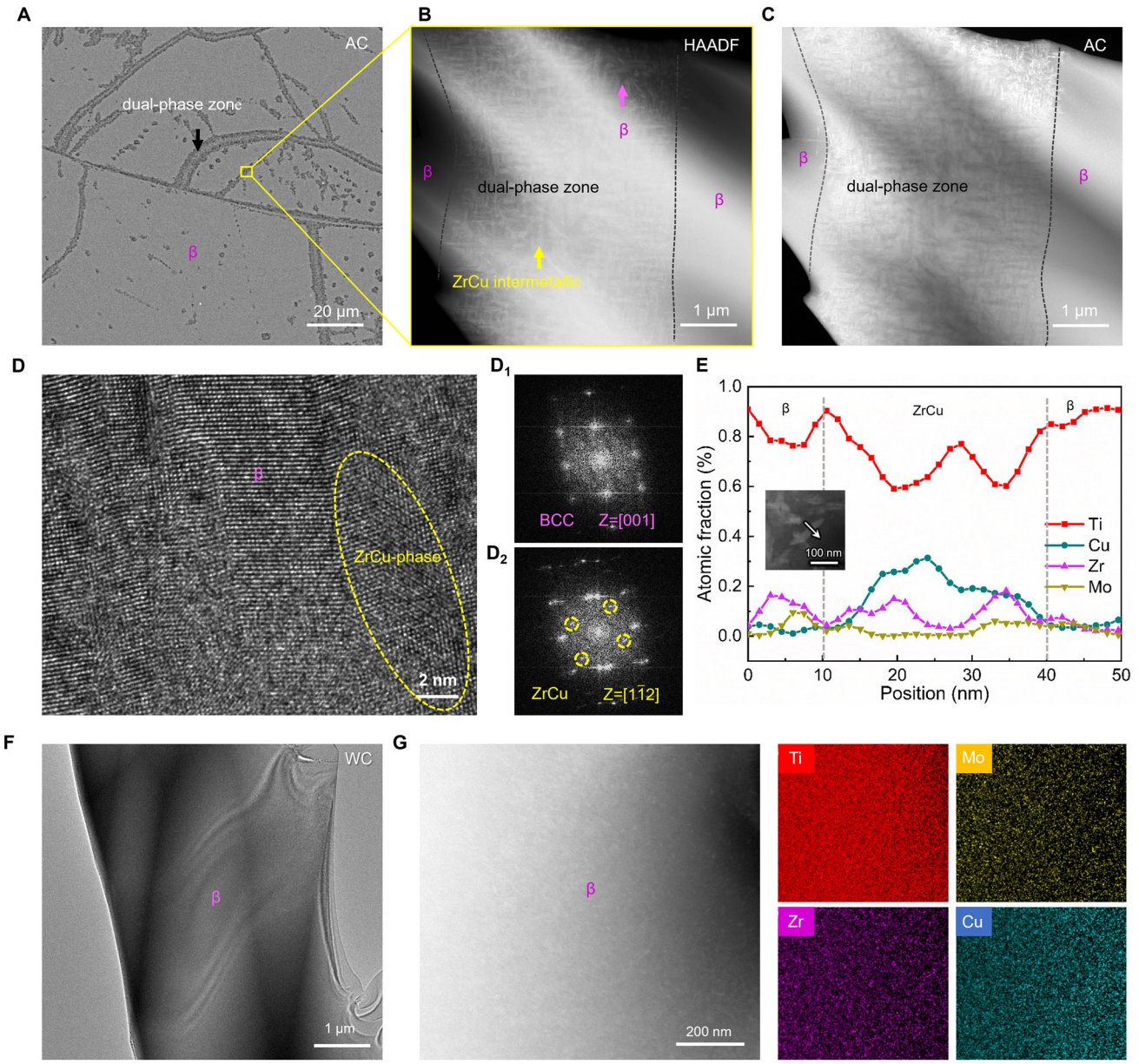


**Fig. 3** TEM characterization of the **A**–**E** AC and **F**, **G** WC alloys. **A** SEM, HAADF, and DF images, showing the substructures of the AC alloy. **D** High-resolution (HR) TEM image, giving a clear atomic arrangement of ZrCu intermetallic. $\mathbf{D_1}$, $\mathbf{D_2}$ Corresponding FFT patterns of β-Ti and ZrCu intermetallic, respectively. **E** Projected one-dimensional concentration profile along with a white arrow in the inset. **F**, **G** STEM, DF images, and EDS maps of the WC alloy

### *3.2.1 Deformation mechanisms*

Based on the study of Sharma et al. [42], the phase structures and their atomic distribution significantly impact elastic moduli. To understand the mechanism of plastic deformation in the annealing MEAs, it is insightful to examine the deformation mechanisms. Figure 5 presents TEM images from deformed MEAs. Deformation occurs mainly by dislocation activity up to fracture in all samples. In the AS alloy, high-density dislocations are hindered by dispersed ZrCu precipitates (Fig. 5A). The dislocation structure is characterized by a configuration of planar glide along one slip system, forming high-density dislocation walls with a spacing distance of 100 nm (Fig. 5B). These dislocation walls play a dominant role in the work hardening by acting as barriers for the motion of dislocations inside them. Distinct from the AS alloy, an extra α precipitate with hundreds of nanometers further impedes the motions of dislocations, contributing a strong increase in the strength of FC alloy but poor plasticity (Fig. 5C). At a

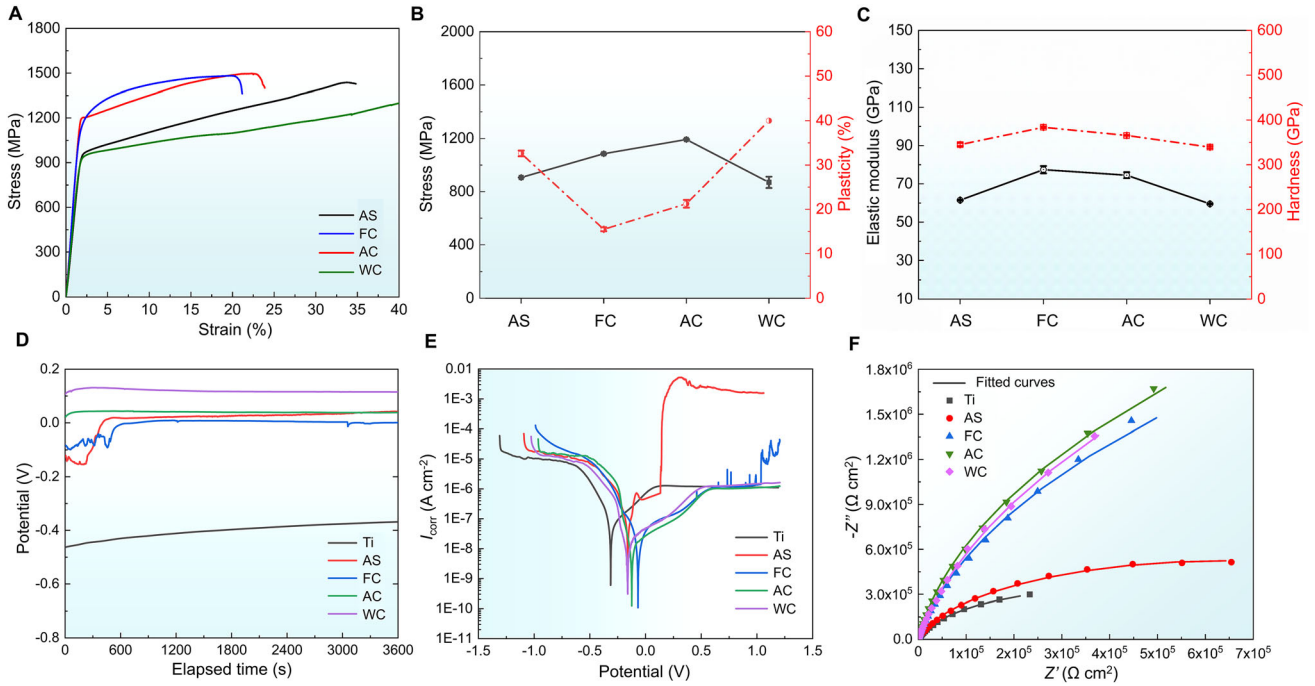


**Fig. 4** The mechanical properties of Ti–18Zr–8Mo–10Cu MEAs: **A** compressive stress–strain curves; **B** yield strength and plasticity variations; and **C** modulus and microhardness variations. Electrochemical characterization: **D** open-circuit potential OCP curves; **E** potentiodynamic polarization curves; and **F** Nyquist plot diagram

higher cooling rate (the AC alloy), the ZrCu precipitates gather around the grain boundaries (Fig. 5D, E). Strain accumulation occurs near the interface between the ZrCu phases and the BCC matrix [43], also showing a limited plasticity. Meanwhile, it evidences that grain boundaries act as low-energy heterogeneous nucleation sites to destabilize the supersaturated Ti-MEAs [44]. After water cooling (the WC alloy), a single β matrix shows a high density of dislocations via BF image in Fig. 5F. Notably, the nodes of the dislocation tangles in this region may act as Frank–Read sources, emitting new dislocations into the surrounding matrix. Cross-slips and interactions occur between these newly formed dislocations [45], which mainly contribute to the high ductility of the MEA.

### *3.2.2 Damage characteristics*

The fracture behaviors of Ti–18Zr–8Mo–10Cu MEAs were investigated to reveal the effects of phase transformation. Figure S2 illustrates the fracture surface of the four type alloys. The fracture surfaces of the AS, FC, and AC alloys (Fig. S2A–C) exhibit numerous cleavage planes, indicating a brittle fracture pattern. In contrast, the WC alloy (Fig. S2D) remains intact, showing many secondary cracks and no major crack fracture is generated, resulting in a ductile fracture pattern. Hence, the WC alloy demonstrates an exceptional balance between strength and ductility.

## 3.3 Antibacterial performance

In addition to their mechanical properties, biocompatibility also plays a key role in the design of bio-MEAs. The antibacterial efficacy of Ti–18Zr–8Mo–10Cu MEAs was initially assessed through incubation with *E. coli* at various time intervals (3, 12, and 24 h). This was followed by an evaluation of bacterial colony formation to quantify the antibacterial rate. In comparison with Ti, the Ti–18Zr–8Mo–10Cu MEAs exhibited a significantly reduced number of *E. coli* colonies across all time intervals (Fig. 6A). After a 3-h incubation with *E. coli*, the WC MEA demonstrates an antibacterial rate comparable to that of the AS alloy (Fig. 6B), indicating that the water-cooling process did not substantially alter the antibacterial properties of the as-cast Ti–18Zr–8Mo–10Cu alloy. Furthermore, a marginally higher number of bacterial colonies are observed in the AC alloy compared to the AS alloy. This suggests that the more homogeneous solid solution of Cu within the alloy matrix slightly diminishes the antibacterial efficacy of the Ti–18Zr–8Mo–10Cu alloy. In contrast, the FC specimen, primarily consisting of granular ZrCu precipitates, demonstrates a superior antibacterial rate relative to the other alloys (Fig. 6B), implying that the ZrCu phase confers significant antibacterial properties. Notably, at both 12 and 24 h, all MEAs achieve an antibacterial rate of 100%. These findings indicate that Ti–18Zr–8Mo–10Cu

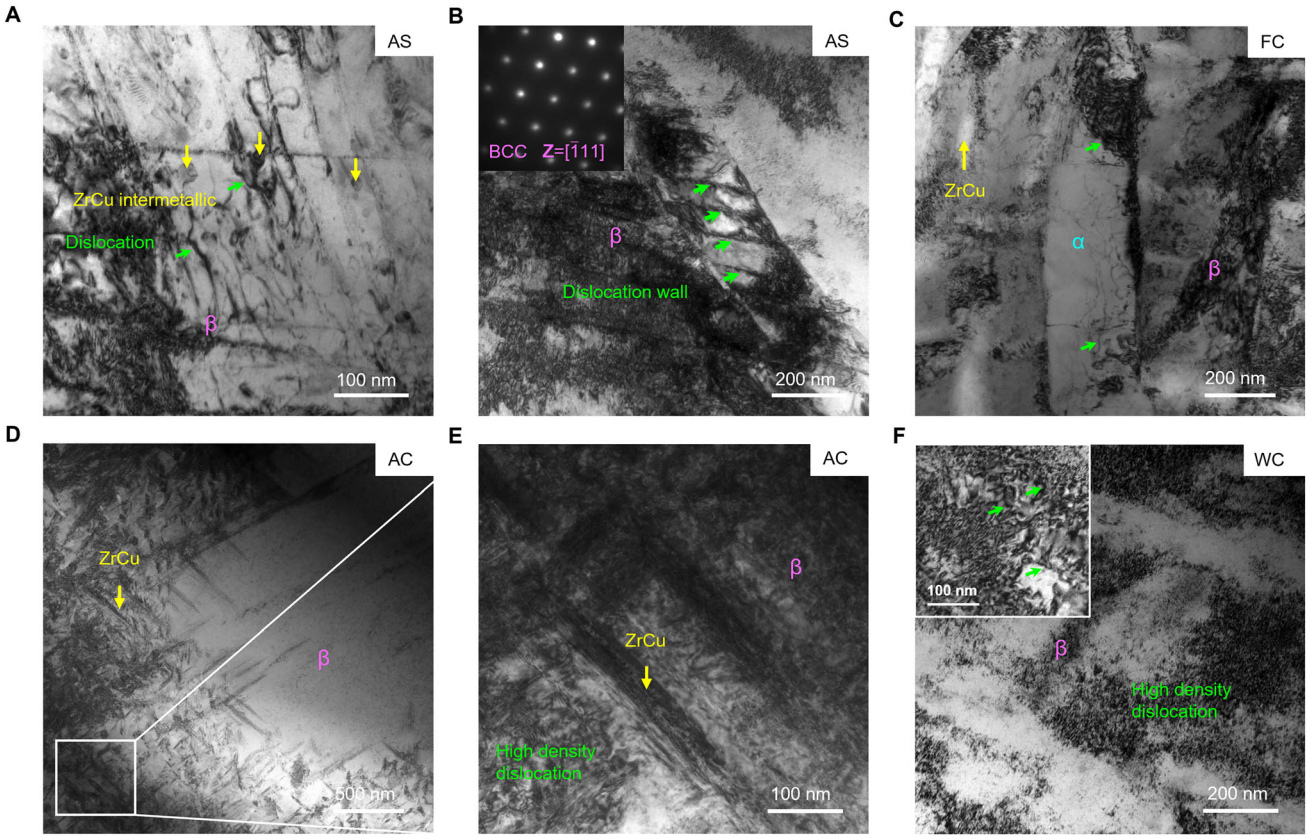


**Fig. 5** The bright-field TEM images of defect structures. **A**, **B** AS alloy, inset: the corresponding SAED patterns; **C** FC alloy; **D**, **E** AC alloy; and **F** WC alloy, inset: enlarged dislocations

MEAs exhibit exceptional antibacterial properties (> 99%) after various heat treatments. This observation aligns well with THE previous studies on the antibacterial efficacy of Cu-bearing Ti alloys with comparable Cu content [17, 46].

The morphology and viability of *E. coli* cultured on the surface of Ti–18Zr–8Mo–10Cu MEAs were examined using SEM and live/dead staining techniques, respectively. After 24 h of incubation, a substantial number of normal rod-shaped *E. coli* are observed in the Ti alloy, with some forming confluent colonies, as indicated by the red arrows in Fig. 6C. Conversely, a limited number of *E. coli* clones are detected on the surface of Ti–18Zr–8Mo–10Cu MEAs. The structural integrity of the bacteria is compromised on these MEAs, as evidenced by the rupture of the cell membrane and subsequent efflux of cytoplasm (Fig. 6D). These findings suggest that Ti–18Zr–8Mo–10Cu MEAs possess a significant capacity to inhibit bacterial adhesion and biofilm formation. Notably, the FC specimen exhibited reduced bacterial adhesion compared to other alloys, with almost no intact bacteria observed, indicating superior antibacterial efficacy. In Cu-bearing titanium alloys, Cu ion-mediated membrane disruption and ROS generation are well-documented mechanisms for their antibacterial performance [47–50]. According to the SEM results (Fig. 6D), it is evident that Cu ion-mediated membrane disruption contributed to the antibacterial property of Ti–18Zr–8Mo–10Cu MEAs, but whether the antibacterial process was related to ROS generation remains further investigation. Based on the results of live/dead staining (Fig. 6E), a higher prevalence of live *E. coli* (indicated by green fluorescence) is observed in the Ti alloy, whereas a greater number of dead bacterial (indicated by red fluorescence) are detected in the Ti–18Zr–8Mo–10Cu MEAs. Notably, nearly all *E. coli* are found to be dead on the FC alloy surface, demonstrating substantial antibacterial efficacy, which is consistent with the results of the antibacterial rate. Furthermore, the antibacterial efficiency of Ti–18Zr–8Mo–10Cu MEAs was comparable to that of some HEAs such as $Cu_{40}Zn_{24}Ni_{24}Ag_8Hg_4$ [51] showing an antibacterial rate of 100% after the incubation with bacterial for 12 h in vitro (Fig. 6B).

Figure S3 illustrates the cumulative release of Cu ions from Ti–18Zr–8Mo–10Cu MEAs immersed in deionized water. During the initial 72 h, the release of Cu ions increased rapidly, followed by a more gradual release extending up to 168 h. The continuous release of Cu ions ensures the long-term antibacterial efficacy of alloys. After 168 h of immersion, the quantities of released Cu ions in

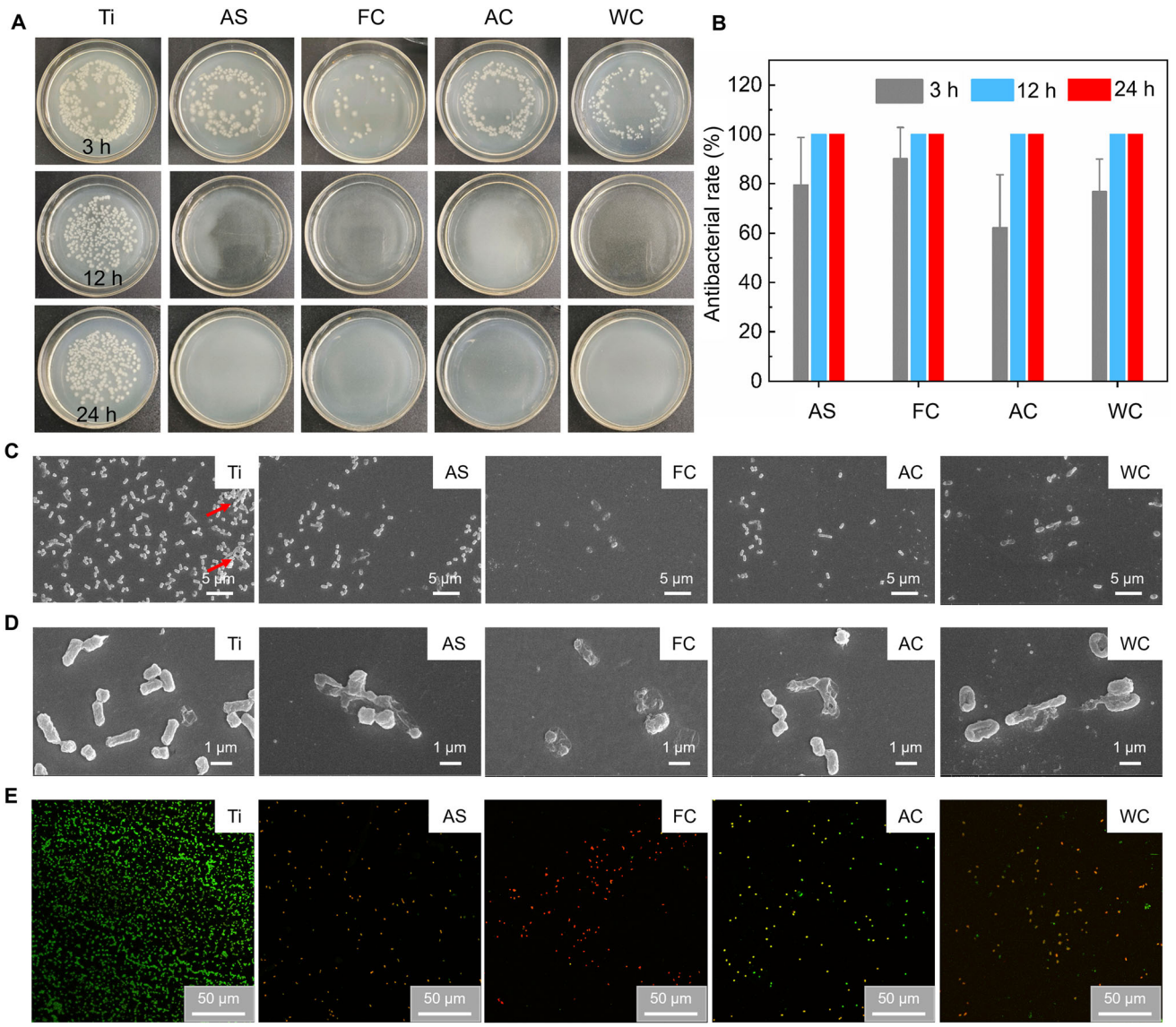


**Fig. 6** The antibacterial rate of Ti–18Zr–8Mo–10Cu MEAs. **A** The colony formation of *E. coli* after culture with Ti–18Zr–8Mo–10Cu MEAs for 3, 12, and 24 h, respectively. Ti served as the control group. **B** The antibacterial rate of Ti–18Zr–8Mo–10Cu MEAs. The morphology and viability of *E. coli* cultured on the surface of Ti–18Zr–8Mo–10Cu MEAs: **C** low magnification; red arrows: confluent colonies; and **D** high magnification. **E** CLSM observation of live/dead staining of *E. coli*. Ti served as the control group

the AS, FC, AC, and WC alloys are $750.09 \pm 4.69$, $351.55 \pm 12.55$, $386.49 \pm 21.13$, and $437.91 \pm 17.8$ μg $L^{-1}$, respectively. Importantly, the amount of released copper ions is significantly lower than the cytotoxic concentration of Cu ions ($9 \times 10^3$ μg $L^{-1}$) [52]. It is well-established that human tissues exhibit lower sensitivity to Cu, whereas microorganisms are highly susceptible to its toxic effects [53]. Therefore, in the design of Cu-containing Ti alloys, it is crucial to balance the antibacterial properties of Cu ions with their cytotoxicity.

After 168 h of immersion, the FC alloy exhibits a reduced cumulative release of Cu ions than the others (Fig. S1). Conversely, its antibacterial efficacy, following a 3-h incubation with *E. coli*, surpasses the other alloys (Fig. 6B). Therefore, there could be another contribution to the antibacterial properties of Ti–18Zr–8Mo–10Cu MEAs. In Ti-Cu alloys, contact sterilization is considered a primary antibacterial mechanism [10, 54]. Based on this mechanism, bacterial eradication occurs upon contact with copper-rich phases. Consequently, it is anticipated that the antibacterial efficacy of Ti–18Zr–8Mo–10Cu MEAs is associated with their copper-rich phases. Examination of the microstructure in the FC alloy reveals extensive surface areas of ZrCu phases (Fig. 1D). Moreover, the ZrCu phases

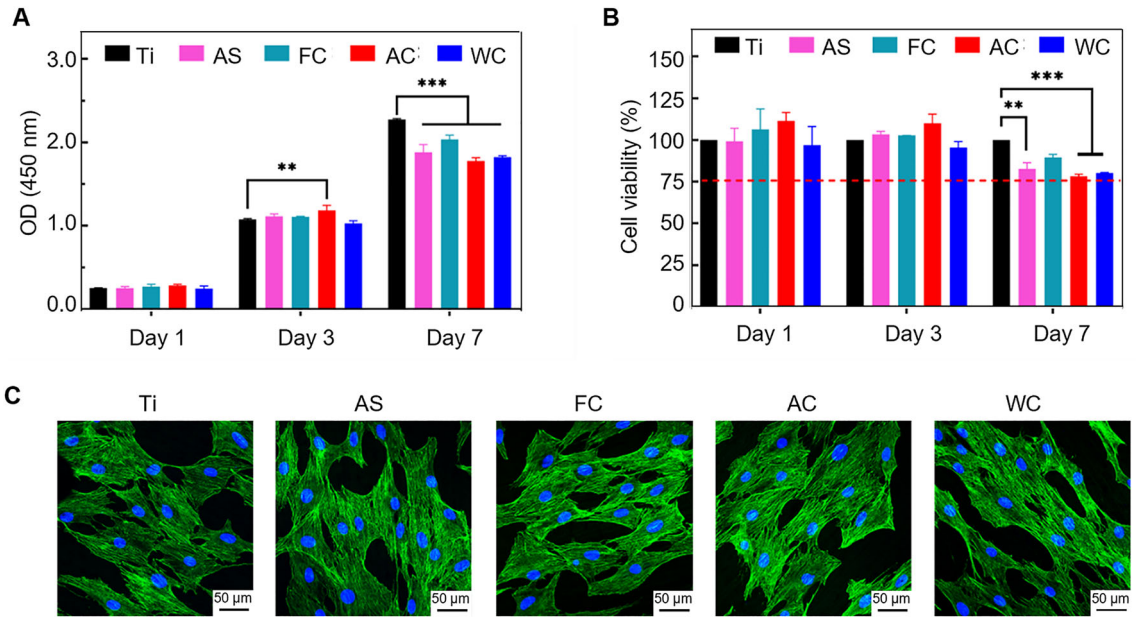


**Fig. 7** Cytocompatibility of Ti–18Zr–8Mo–10Cu MEAs. Proliferation and relative viability of MC3T3-E1 cells cultured on the surface of Ti–18Zr–8Mo–10Cu MEA: **A** CCK-8 assay; **B** relative cell viability; and **C** merged fluorescent images of MC3T3-E1 cultured on the surfaces of alloys. Green fluorescence: cytoskeleton and blue fluorescence: cell nucleus

precipitated in the FC matrix have the potential to form a "micro-galvanic cell" with the α phases, which could further enhance the antibacterial properties of alloys. For example, Xin et al. reported that the formation of a micro-galvanic cell by the $Ti_2Cu$ phase and the α matrix enhances the antibacterial properties of Ti–Cu alloys [38]. Furthermore, the size of Cu-rich phases may also influence the antibacterial properties of Ti–18Zr–8Mo–10Cu MEAs. In the AC alloy, the average size of the needle-like ZrCu precipitates is small (Fig. 3A-C), which makes it difficult to effectively inhibit the growth of bacteria adhered to the surface of the alloys. Consequently, the antibacterial properties of the AC MEA are weaker than those of the AS alloy that exhibits larger Cu-rich phases. Similarly, Cao et al. noted that smaller Ag nanoparticles exhibit weaker antibacterial activity compared to larger ones, which is attributed to their smaller contact area [55].

### 3.4 Cytocompatibility

The cytocompatibility of Ti–18Zr–8Mo–10Cu MEAs was evaluated through the proliferation and morphology of MC3T3-E1 cells cultured on the alloy surfaces. In each alloy, cell proliferation is robust, as indicated by a progressively increasing optical density value with extended culture duration (Fig. 7A). At early time points, the Ti–18Zr–8Mo–10Cu MEAs demonstrated cell proliferation rates comparable to or exceeding those in the Ti specimen, potentially attributable to the positive influence of copper ions on osteoblast proliferation [56]. However, by day 7, the Ti–18Zr–8Mo–10Cu MEAs exhibit reduced proliferation relative to the Ti alloy. This observation aligns with the results of a prior study conducted by Zhang et al. [57], which can be explained by the ability of Cu ions to enhance the early osteogenic differentiation of MC3T3-E1 cells. Using the cell viability of Ti as a baseline of 100%, no significant differences were observed between Ti and Ti–18Zr–8Mo–10Cu MEAs on days 1 and 3; furthermore, the relative viability of Ti–18Zr–8Mo–10Cu MEAs exceeded 75% on day 7 (Fig. 7B), which is classified as non-cytotoxic (grade 1 cytotoxicity) according to established cell toxicity standards [58].

Figure 7C illustrates the morphology of MC3T3-E1 cells cultured on the surface of Ti–18Zr–8Mo–10Cu MEAs for 24 h. There is no significant difference in the morphology and number of MC3T3-E1 cells between the Ti–18Zr–8Mo–10Cu MEAs and Ti. Generally, the cells exhibit an elongated or spindle-shaped morphology, and their pseudopods form junctions to facilitate intercellular communication. These results indicate that Ti–18Zr–8Mo–10Cu MEAs are conducive to the adhesion and spreading of MC3T3-E1 cells on their surfaces. Collectively, it is evident that Ti–18Zr–8Mo–10Cu MEAs do not exhibit any significant cytotoxic effects, which is similar to the previous reports [59]. Therefore, they meet the requirements for biomedical applications.

## 4 Conclusion

Through a comprehensive investigation of Ti–18Zr–8Mo–10Cu MEAs prepared by different heat treatments. The cooling methods significantly affect phase structure, precipitation behavior, microstructure, and elemental distribution in Ti–18Zr–8Mo–10Cu MEAs. Specifically, the AS and AC alloys exhibit both the β-phase and the intermetallic ZrCu phase, while the FC specimen displays the β, ZrCu, and α phases. Only WC alloy stabilizes the single β-phase, highlighting the potential for broader biomedical applications. The microstructural variations induced by heat treatment have a direct impact on the mechanical properties of Ti–18Zr–8Mo–10Cu MEAs. With an increasing cooling rate, the microhardness and elastic modulus decrease. The WC alloy displays optimal ductility, whereas the FC alloy exhibits a significant reduction in elongation. Moreover, the WC alloys possess superior corrosion resistance than Ti. The synthesized Ti–18Zr–8Mo–10Cu MEAs exhibit remarkable antibacterial properties and outstanding cytocompatibility, primarily attributed to the presence of Cu-rich precipitates. An increasing surface area of the Cu-rich phase significantly contributes to their antibacterial efficacy. Owing to its advantageous combination of strength, ductility, elastic modulus, corrosion resistance, antibacterial properties, and cytocompatibility, the water-cooling alloy exhibits substantial potential for future applications in orthopedics.

**Acknowledgements** This study was financially supported by the National Natural Science Foundation of China (Nos. 52231005 and 52001324), the Start-up Research Fund of Southeast University (No. RF1028623113), and the Laboratory of Advanced Metallic Materials, Southeast University (Nos. AMM2025A01, AMM2024A02, and AMM2023B05), and the Natural Science Foundation of Henan Province (No. 252300421541).

**Author contributions** Zhi-Jun Guo helped in methodology; investigation; data curation; writing—review and editing, and funding acquisition. Yu-Sha Luo helped in data curation; visualization; writing—original draft; and writing—review and editing. Min-Qi Xu helped in methodology; investigation; and writing—original draft. Min-Tao Xue helped in formal analysis and investigation. Bian-Yun Cai helped in investigation. Yi-Zhou Huang helped in investigation; writing—original draft; and writing—review and editing. Bao-Long Shen worked in supervision; project administration; and funding acquisition.

**Data availability** The data that support the findings of this study are available from the corresponding author upon reasonable request.

### Declarations

**Conflict of interests** The authors declare that they have no conflict of interest.

## References

[1] Chen QZ, Thouas GA. Metallic implant biomaterials. Mater Sci Eng R Rep. 2015;87:1–57. https://doi.org/10.1016/j.mser.2014.10.001.

[2] Rasouli MR, Restrepo C, Maltenfort MG, James J, Parvizi J. Risk factors for surgical site infection following total joint arthroplasty. J Bone Joint Surg Am. 2014;96(18):e158. https://doi.org/10.2106/jbjs.m.01363.

[3] McHendrie R, Nguyen NH, Nguyen MT, Fallahnezhad K, Vasilev K, Truong VK, Hashemi R. Development of novel antibacterial Ti–Nb–Ga alloys with low stiffness for medicalimplant applications. J Funct Biomater. 2024;15(6): 167. https://doi.org/10.3390/jfb15060167.

[4] Ma TY, Ran TF, Ke S, Qin YY. The antibacterial activity comparison between novel carbon-based nanofilm coated titanium alloy and Co–Cr–Mo alloy. Evid Based Complement Alternat Med. 2022;30(1):5463383. https://doi.org/10.1155/2022/5463383.

[5] Kessler B, Sendi P, Graber P, Knupp M, Zwicky L, Hintermann B, Zimmerli W. Risk factors for periprosthetic ankle joint infection: a case-control study. J Bone Joint Surg Am. 2012;94(20):1871–6. https://doi.org/10.2106/jbjs.k.00593.

[6] Laffer RR, Graber P, Ochsner PE, Zimmerli W. Outcome of prosthetic knee-associated infection: evaluation of 40 consecutive episodes at a single centre. Clin Microbiol Infect. 2006;12(5):433–9. https://doi.org/10.1111/j.1469-0691.2006.01378.x.

[7] Anguita-Alonso P, Hanssen AD, Osmon DR, Trampuz A, Steckelberg JM, Patel R. High rate of aminoglycoside resistance among staphylococci causing prosthetic joint infection. Clin Orthop Relat Res. 2005;439:43–7. https://doi.org/10.1097/01.blo.0000182394.39601.9d.

[8] Khan MS, Rehman S, Ali MA, Sultan B, Sultan S. Infection in orthopedic implant surgery, its risk factors and outcome. J Ayub Med Coll Abbottabad. 2008;20(1):23–5.

[9] Sohail MR, Henrikson CA, Braid-Forbes MJ, Forbes KF, Lerner DJ. Mortality and cost associated with cardiovascular implantable electronic device infections. Arch Intern Med. 2011;171(20):1821–8. https://doi.org/10.1001/archinternmed.2011.441.

[10] Zhang EL, Li FB, Wang HY, Liu J, Wang CM, Li MQ, Yang K. A new antibacterial titanium-copper sintered alloy: preparation and antibacterial property. Mater Sci Eng C Mater Biol Appl. 2013;33(7):4280–7. https://doi.org/10.1016/j.msec.2013.06.016.

[11] Boutinguiza M, Fernández-Arias M, del Val J, Buxadera-Palomero J, Rodríguez D, Lusquiños F, Gil FJ, Pou J. Synthesis and deposition of silver nanoparticles on cp Ti by laser ablation in open air for antibacterial effect in dental implants. Mater Lett. 2018;231(15):126–9. https://doi.org/10.1016/j.matlet.2018.07.134.

[12] Guo LT, Feng WM, Liu X, Lin C, Li B, Qiang YH. Sol-gel synthesis of antibacterial hybrid coatings on titanium. Mater Lett. 2015;160(1):448–51. https://doi.org/10.1016/j.matlet.2015.08.027.

[13] Silva FS, Cinca N, Dosta S, Cano IG, Guilemany JM, Caires CSA, Lima AR, Silva CM, Oliveira SL, Caires ARL, Benedetti AV. Corrosion resistance and antibacterial properties of copper coating deposited by cold gas spray. Surf Coat Tech. 2019;361(15):292–301. https://doi.org/10.1016/j.surfcoat.2019.01.029.

[14] Jin XM, Gao LZ, Liu EQ, Yu FF, Shu XF, Wang HF. Microstructure, corrosion and tribological and antibacterial properties of Ti–Cu coated stainless steel. J Mech Behav Biomed Mater. 2015;50:23–32. https://doi.org/10.1016/j.jmbbm.2015.06.004.

[15] Wang JW, Zhang SY, Sun ZQ, Wang H, Ren L, Yang K. Optimization of mechanical property, antibacterial property and corrosion resistance of Ti–Cu alloy for dental implant. J Mater Sci Technol. 2019;35(10):2336–44. https://doi.org/10.1016/j.jmst.2019.03.044.
[16] Peng C, Zhang SY, Sun ZQ, Ren L, Yang K. Effect of annealing temperature on mechanical and antibacterial properties of Cu-bearing titanium alloy and its preliminary study of antibacterial mechanism. Mater Sci Eng C Mater Biol Appl. 2018;93(1):495–504. https://doi.org/10.1016/j.msec.2018.08.018.
[17] Ke ZY, Yi CB, Zhang L, He ZY, Tan J, Jiang YH. Characterization of a new Ti–13Nb–13Zr–10Cu alloy with enhanced antibacterial activity for biomedical applications. Mater Lett. 2019;253(15):335–8. https://doi.org/10.1016/j.matlet.2019.07.008.
[18] Hua NB, Wang WJ, Wang QT, Ye YX, Lin SH, Zhang L, Guo QH, Brechtl J, Liaw PK. Mechanical, corrosion, and wear properties of biomedical Ti–Zr–Nb–Ta-Mo high entropy alloys. J Alloy Compd. 2021;861(25):157997. https://doi.org/10.1016/j.jallcom.2020.157997.
[19] Li WD, Xie D, Li DY, Zhang Y, Gao YF, Liaw PK. Mechanical behavior of high-entropy alloys. Prog Mater Sci. 2021;118:100777. https://doi.org/10.1016/j.pmatsci.2021.100777.
[20] Yan XL, Guo H, Yang W, Pang SJ, Wang Q, Liu Y, Liaw PK, Zhang T. $Al_{0.3}$CrxFeCoNi high-entropy alloys with high corrosion resistance and good mechanical properties. J Alloy Compd. 2021;860(15):158436. https://doi.org/10.1016/j.jallcom.2020.158436.
[21] Yang W, Pang Sj, Liu Y, Wang Q, Liaw PK, Zhang T. Design and properties of novel Ti-Zr-Hf-Nb-Ta high-entropy alloys for biomedical applications. Intermetallics. 2022;141:107421. https://doi.org/10.1016/j.intermet.2021.107421.
[22] Yuan Y, Wu Y, Yang Z, Liang X, Lei ZF, Huang HL, Wang H, Liu XJ, An K, Wu W, Lu ZP. Formation, structure and properties of biocompatible TiZrHfNbTa high-entropy alloys. Mater Res Lett. 2019;7(6):225–31. https://doi.org/10.1080/21663831.2019.1584592.
[23] Nagase T, Mizuuchi K, Nakano T. Solidification microstructures of the ingots obtained by arc melting and cold crucible levitation melting in TiNbTaZr medium-entropy alloy and TiNbTaZrX (X=V, Mo, W) high-entropy alloys. Entropy. 2019;21(5):483. https://doi.org/10.3390/e21050483.
[24] Nagase T, Iijima Y, Matsugaki A, Ameyama K, Nakano T. Design and fabrication of Ti-Zr-Hf-Cr-Mo and Ti–Zr–Hf–-Co–Cr–Mo high-entropy alloys as metallic biomaterials. Mater Sci Eng C Mater Biol Appl. 2020;107:110322. https://doi.org/10.1016/j.msec.2019.110322.
[25] Hua ZL, Zhang DC, Guo L, Lin SH, Li YC, Wen C. Medium-entropy Zr-Nb-Ti alloys with low magnetic susceptibility, high yield strength, and low elastic modulus through spinodal decomposition for bone-implant applications. Acta Biomater. 2024;190:623–41. https://doi.org/10.1016/j.actbio.2024.11.001.
[26] Wang SB, Wu DL, She H, Wu MX, Shu D, Dong AP, Lai HC, Sun BD. Design of high-ductile medium entropy alloys for dental implants. Mater Sci Eng C Mater Biol Appl. 2020;113:110959. https://doi.org/10.1016/j.msec.2020.110959.
[27] Zhang Y, Liu Y, Zheng RN, Zheng YQ, Chen LS. Research progress on corrosion behaviors and biocompatibility of rare-earth magnesium alloys in vivo and in vitro. J Rare Earths. 2023;41(12):1827–42. https://doi.org/10.1016/j.jre.2023.03.005.
[28] Hao YL, Li SJ, Prima F, Yang R. Controlling reversible martensitic transformation in titanium alloys with high strength and low elastic modulus. Scr Mater. 2012;67(5):487–90. https://doi.org/10.1016/j.scriptamat.2012.06.011.
[29] Wang HL, Hao YL, He SY, Li T, Cairney JM, Wang YD, Wang Y, Obbard EG, Prima F, Du K, Li SJ, Yang R. Elastically confined martensitic transformation at the nano-scale in a multifunctional titanium alloy. Acta Mater. 2017;135(15):330–9. https://doi.org/10.1016/j.actamat.2017.06.040.
[30] Mohammed MT. Development of a new metastable beta titanium alloy for biomedical applications. KIJOMS. 2017;3(4):224–30. https://doi.org/10.1016/j.kijoms.2017.08.005.
[31] Todai M, Nagase T, Hori T, Matsugaki A, Sekita A, Nakano T. Novel TiNbTaZrMo high-entropy alloys for metallic biomaterials. Scr Mater. 2017;129(1):65–8. https://doi.org/10.1016/j.scriptamat.2016.10.028.
[32] Hori T, Nagase T, Todai M, Matsugaki A, Nakano T. Development of non-equiatomic Ti–Nb–Ta–Zr–Mo high-entropy alloys for metallic biomaterials. Scr Mater. 2019;172:83–7. https://doi.org/10.1016/j.scriptamat.2019.07.011.
[33] Hao YL, Li SJ, Sun SY, Zheng CY, Yang R. Elastic deformation behaviour of Ti–24Nb–4Zr–7.9Sn for biomedical applications. Acta Biomater. 2007;3(2):277–86. https://doi.org/10.1016/j.actbio.2006.11.002.
[34] Zhong Q, Pan X, Chen YH, Lian Q, Gao J, Xu YX, Wang J, Shi ZJ, Cheng H. Prosthetic metals: release, metabolism and toxicity. Int J Nanomedicine. 2024;19:5245–67. https://doi.org/10.2147/ijn.s459255.
[35] Ma W, Huang H, Ding W, Guo S, Liu HX, Cheng XH. Near-linear elastic deformation behavior of a novel Zr–Ti-Nb–Sn alloy with multi-phase microstructures of β, α″ and α′ phases. Rare Met. 2023;42:1670–7. https://doi.org/10.1007/s12598-023-02287-z.
[36] Yu SY, Brodrick CW, Ryan MP, Scully JR. Effects of Nb and Zr alloying additions on the activation behavior of Ti in hydrochloric acid. J Electrochem Soc. 1999;146(12):4429.
[37] He ZY, Xu JX, Cao FH, Pan JH, Li DY, Fang ZJ, Li YM. Correlation between microstructural evolution and ultrasonic propagation behavior in extra-low-interstitial-grade Ti6Al4V alloys. Rare Met. 2025;44:5781–92. https://doi.org/10.1007/s12598-025-03270-6.
[38] Xin C, Wang N, Chen YN, He BB, Zhao QY, Chen L, Tang YF, Luo BL, Zhao YQ, Yang XK. Biological corrosion behaviour and antibacterial properties of Ti–Cu alloy with different $Ti_2Cu$ morphologies for dental applications. Mater Des. 2022;215:110540. https://doi.org/10.1016/j.matdes.2022.110540.
[39] Annur D, Bilbusyra SF, Nuraini L, Sutowo C, Senopati G, Gusnaniar N, Widiyarti G, Prajatelistiya E, Thaha YN. Microstructure, mechanical properties, and corrosion behavior of novel antibacterial Ti-25Nb-*x*Cu for dental implant. Phys Scr. 2025;100(3):035026. https://www.x-mol.com/paperRedirect/1894084857070968832.
[40] Pan J, Thierry D, Leygraf C. Electrochemical impedance spectroscopy study of the passive oxide film on titanium for implant application. Electrochim Acta. 1996;41(7–8):1143–53. https://doi.org/10.1016/0013-4686(95)00465-3.
[41] Modi SR, Jha K. A comparative investigation on mechanical and electrochemical characteristics of annealed Ti-6Al-4V ELI with other grades of titanium alloys. J Mater Eng Perform. 2024. https://doi.org/10.1007/s11665-024-10190-6.
[42] Sharma P, Tucker WC, Balasubramanian G. Optimal interplay of charge localization, lattice dynamics and slip systems drives structural softening in dilute W alloys with Re additives. Int J Refract Met Hard Mater. 2025;128:107086. https://doi.org/10.1016/j.ijrmhm.2025.107086.
[43] Wang ML, Lu YP, Lan JG, Wang TM, Zhang C, Cao ZQ, Li TJ, Liaw PK. Lightweight, ultrastrong and high thermal-stable eutectic high-entropy alloys for elevated-temperature applications. Acta Mater. 2023;248:118806. https://doi.org/10.1016/j.actamat.2023.118806.
[44] Tong Y, Chen D, Han B, Wang J, Feng R, Yang T, Zhao C, Zhao YL, Guo W, Shimizu Y, Liu CT, Liaw PK, Inoue K, Nagai

Y, Hu A, Kai JJ. Outstanding tensile properties of a precipitation-strengthened $FeCoNiCrTi_{0.2}$ high-entropy alloy at room and cryogenic temperatures. Acta Mater. 2019;165(15):228–40. https://doi.org/10.1016/j.actamat.2018.11.049.

[45] An ZB, Mao SC, Vayyala A, Yang LY, Jiang C, Shi CJ, Liu Y, Zhou H, Liao XZ, Zhang Z, Han XD. Multiscale hierarchical heterostructure yields combined high strength and excellent ductility in a Co-Cr-Fe-Ni-Al negative enthalpy alloy. Acta Mater. 2024;281(1):120366. https://doi.org/10.1016/j.actamat.2024.120366.

[46] Xie CX, Li W, Zheng DH, Wang KW, Yang YZ, Shen FH, Xie L, Liao ZL, Zhong SY. Study of crystallization behavior and kinetics of magnetic FeCoCrNiZr high entropy amorphous alloy. Non-Cryst Solids. 2019;514(15):20–4. https://doi.org/10.1016/j.jnoncrysol.2019.03.039.

[47] Li M, Ma Z, Zhu Y, Xia H, Yao MY, Chu X, Wang XL, Yang K, Yang MY, Zhang Y, Mao CB. Toward a molecular understanding of the antibacterial mechanism of copper-bearing titanium alloys against *Staphylococcus aureus*. Adv Healthc Mater. 2016;5(5):557–66. https://doi.org/10.1002/adhm.201500712.

[48] Xu JW, Lu YJ, Pan XY, Zhan DS, Wang Q, Zhang N. Antibacterial performance of a porous Cu-bearing titanium alloy by laser additive manufacturing. Front Bioeng Biotechnol. 2023;11:1226745. https://doi.org/10.3389/fbioe.2023.1226745.

[49] Chen JH, He Z, Zheng SL, Gao W, Wang YX. Ultrasonic-assisted electrodeposition of Cu-$TiO_2$ nanocomposite coatings with long-term antibacterial activity. ACS Appl Mater Interfaces. 2024;16(48):66695–705. https://www.x-mol.com/paperRedirect/1859412083353153536.

[50] Liu R, Tang YL, Zeng LL, Zhao Y, Ma Z, Sun ZQ, Xiang LB, Ren L, Yang K. In vitro and in vivo studies of antibacterial copper-bearing titanium alloy for dental application. Dent Mater. 2018;34(8):1112–26. https://doi.org/10.1016/j.dental.2018.04.007.

[51] Sharma P, Rohila S, Hasan U, Krishna PH, Ugwuegbu C, Tiwari A, Joshi M. Multiscale modeling-driven synthesis of $Cu_{40}Zn_{24}Ni_{24}Ag_8Hg_4$ high entropy alloy with antibacterial properties. Nano-Struct Nano-Objects. 2024;40:101391. https://doi.org/10.1016/j.nanoso.2024.101391.

[52] Fowler L, Engqvist H, Öhman-Mägi C. Effect of copper ion concentration on bacteria and cells. Materials. 2019;12(22):3798. https://doi.org/10.3390/ma12223798.

[53] O'Gorman J, Humphreys H. Application of copper to prevent and control infection. Where are we now? J Hosp Infect. 2012;81(4):217–23. https://doi.org/10.1016/j.jhin.2012.05.009.

[54] Guo ZJ, Huang YZ, Sun CC, He ZX, Li YF, Qiu H, Yuan DL, Shen BL. Preparation and characterization of metastable β-type titanium alloys with favorable properties for orthopedic applications. J Alloys Compd. 2023;949(15):169839. https://doi.org/10.1016/j.jallcom.2023.169839.

[55] Cao HL, Qiao YQ, Liu XY, Lu T, Cui T, Meng FH, Chu PK. Electron storage mediated dark antibacterial action of bound silver nanoparticles: smaller is not always better. Acta Biomater. 2013;9(2):5100–10. https://doi.org/10.1016/j.actbio.2012.10.017.

[56] Burghardt I, Luthen F, Prinz C, Kreikemeyer B, Zietz C, Neumann HG, Rychly J. A dual function of copper in designing regenerative implants. Biomaterials. 2015;44:36–44. https://doi.org/10.1016/j.biomaterials.2014.12.022.

[57] Zhang W, Zhang SY, Liu H, Ren L, Wang Q, Zhang Y. Effects of surface roughening on antibacterial and osteogenic properties of Ti–Cu alloys with different Cu contents. J Mater Sci Technol. 2021;88(20):158–67. https://doi.org/10.1016/j.jmst.2021.01.067.

[58] Liu R, Memarzadeh K, Chang B, Zhang YM, Ma Z, Allaker RP, Ren L, Yang K. Antibacterial effect of copper-bearing titanium alloy (Ti-Cu) against *Streptococcus mutans* and *Porphyromonas gingivalis*. Sci Rep. 2016;6:29985. https://doi.org/10.1038/srep29985.

[59] Zhang J, Ren L, Yang K. Cytotoxicity of Ti–6Al–4V–5Cu alloy to MC3T3-E1 cells. Acta Metall Sin. 2020;34:694–700. https://doi.org/10.1007/s40195-020-01158-1.